Electrocatalysis (2017) 8:340–350
DOI 10.1007/s12678-017-0376-8

ORIGINAL RESEARCH

Electrocatalytic Oxidation of Glucose at Nickel Phosphate Nano/Micro Particles Modified Electrode

Mohammed A. Al-Omair[1] · **A. H. Touny**[1,2] · **Faisal A. Al-Odail**[1] · **M. M. Saleh**[1,3]

Published online: 1 May 2017

Abstract Here is a first study of the electrocatalytic oxidation of glucose by nickel phosphate nano/micro particles (NiPh) modified glassy carbon electrode (NiPh/GC). The NiPh is fabricated by a simple reflux method. The morphology and structure of the NiPh particles have been studied using field emission scanning electron microscopy (FE-SEM), X-ray diffraction (XRD), BET surface area measurement and Fourier transfer Infrared spectroscopy (FTIR). According to the above measurements, a needle-like morphology with average particle dimensions of 200 × 800 nm is obtained. The phase structure of the NiPh particles is found to be $Ni_3(PO_4)_2.8H_2O$ and having BET surface area of 20.0 m^2/g. Electrochemical measurements like cyclic voltammetry (CV) are used to characterize the NiPh/GC electrode. Potential cycling in the range of −0.1 to 0.7 V (Ag/AgCl/KCl(sat)) is used to activate the phosphate matrix. After ~75 cycles, two redox peaks are emerged which were assigned for the redox transform NiPh (II)/NiPh (III) due to invasion of the OH^- ions into the NiPh matrix. The NiPh/GC demonstrates electrocatalytic activity towards glucose oxidation in alkaline solution. The glucose reaction is analyzed and characterized in the light of the collected experimental data.

✉ A. H. Touny
atouny@yahoo.com; aahamed@kfu.edu.sa

✉ M. M. Saleh
mmsaleh@kfu.edu.sa; mahmoudsaleh90@yahoo.com

[1] Chemistry Department, College of Science, King Faisal University, Al-Hassa Riyadh, Kingdom of Saudi Arabia

[2] Department of Chemistry, Faculty of Science, Helwan University, Helwan, Egypt

[3] Department of Chemistry, Faculty of Science, Cairo University, Cairo, Egypt

Keywords Nickel phosphate · Particles · Glucose · Electrocatalytic · Oxidation

Introduction

Electrocatalytic oxidation of glucose is extremely important in the application of biosensors and biochemical fuel cells. Fabrication and development of new and efficient catalysts for electrochemical reactions (e.g., glucose oxidation) is a continuous process where it has an interest in the manufacturing of fuel cells and biosensors. The electrooxidation of glucose is of prime importance for the diagnosis of diabetes mellitus, for food preparation processes and for the development of biofuel cells [1–3]. Based on the literature, various reagents have been employed to develop non-enzymatic glucose oxidation. Noble metals such as Pt, Pd and Au are one of these materials that have been extensively used as catalysts for non-enzymatic glucose oxidation owing to their unique electrocatalytic properties, biocompatibility, good electrical and mechanical properties, good electrocatalytic activity and high performance [4, 5]. However, there are some reasons making these materials undesirable. For instance, they are costly and may be susceptible to the poisoning products that emerged during the oxidation process [6, 7]. The above reasons motivated the scientists worldwide to search for replacement for these noble metals. In literatures, there are other materials (metal and metal oxides) that have been also used as catalysts such as NiO_x, FeOOH, MnO_2, RuO_2, CuO_x, ZnO and Co_3O_4. Recently their nanoparticle-based electrodes have been used for glucose oxidation in alkaline solutions [8–10].

Of the above metal oxides, nickel oxides have particular interest because it has been used as a catalyst for several reactions [11, 12]. Most of the Ni-based glucose sensors were fabricated by modifying traditional electrodes with Ni-based

nanomaterials using different techniques. These include (but not limited to) dispersing Ni particles in disordered graphite-like carbon [13], doping of the carbon paste electrode with nano-NiO [14] and casting of NiO particles prepared using a sol-gel technique [15]. Also, nickel-DNA nanocomposites display unique three dimensional structures and represent a potential for new functionalities in the development of biosensors for important biochemical species such as glucose [16–18].

The source of the active Ni (II)/Ni (III) couple (nickel hydroxide/nickel oxyhydroxide) in the above examples, after potential cycling in alkali, are Ni, NiO or Ni $(OH)_2$ and yet introducing that active couple from Ni salt (e.g., nickel phosphate, NiPh) is considered to be scarce [19, 20].

Alloying Pt [21], Pd [22] and more available metal like Ni [23–25] with an inexpensive metalloid element such as phosphorous have been always aimed to increase the electroactivity of electrooxidation of small organic molecules and CO tolerance. Phosphorous has abundant valence electrons and can affect the electronic states of the studied elements via affecting the electronic states of the main metal (e.g., Pt or Ni) [26]. Meanwhile, the presence of the phosphorus atoms may help to adsorb oxygen groups due to the oxophilic nature of the phosphorus [27]. This can result in oxidation of the CO_{ads} to carbon dioxide and hence enhance organic molecules oxidation [28].

Here is the first trial for nickel inorganic compounds bearing redox properties such as NiPh to be evaluated for electrocatalytic oxidation for glucose molecules. Consequently this calls for research to fabricate a targeted catalyst (such as nickel phosphate) to be used for electrocatalytic (non-enzymatic) glucose oxidation.

Metal phosphates represent the core for many technological and industrial considerations since they have considerable chemical stability and catalytic properties [29, 30]. Different applications emerge from using metal phosphates. These include (but not limited to) catalysis in chemical conversion [31, 32], tissue engineering [33, 34], drug delivery [35] and antibacterial activity [36, 37]. Additionally nickel phosphate has been employed in a wide range of uses such as in lithium batteries [38, 39], supercapacitors [40, 41], catalytic reactions [42] and in electrocatalytic reactions [43]. Numerous methods have been found for the synthesis of nickel phosphates including solvothermal [44, 45], hydrothermal [46], wet chemical process [47, 48] and sol-gel technique [49]. The chemical composition, structural and morphological properties are highly dependent on the used fabrication approach. The variation in the properties when using different synthesis techniques directed nickel phosphate to be relevant in different fields of applications [50].

Preparation of nickel phosphate particles in nano- and micro scales using surfactants, ligands or solid membrane templates has been found in literatures [51]. Although the hydrothermal process is a eco-friendly technique and calcination step is not required, it has two major drawbacks. It is costly and time consuming process [52]. Developing a unique synthesis route to obtain similar morphological structures that produced by high temperature hydrothermal process is still a challenging work. To the best of our knowledge, the synthesis of nickel phosphate from its precursor salts via reflux-based method has not been reported. Reflux-based method can handle those drawbacks of the hydrothermal method since it is an efficient technique due to its simplicity and costly effective.

In the present work, nickel phosphate will be fabricated as a new catalyst for glucose oxidation. Several goals will be studied in this work**.** The main goal is to synthesize nickel phosphate (NiPh) with nano to micro scale particles by using reflux approach. The second one is to modify the GC electrode with NiPh to be used in electrocatalytic oxidation of glucose in alkaline solution. The final goal is to study the morphological and structural properties of the NiPh using X-Ray spectroscopy, scanning electron microscope (SEM), BET surface area measurement and FT-IR absorption spectroscopy. The electrochemical and electrocatalytic properties of the NiPh/GC will be studied by cyclic voltammetry (CV).

Experimental

The chemicals were of analytical grade and purchased from Fisher and Sigma-Aldrich and were used as received without further purification. All solutions were prepared using double distilled water.

Material Synthesis

A reflux-based route was used for synthesis of nickel phosphate. A precipitate of nickel phosphate was mainly prepared from nickel nitrate (Ni $(NO_3)_2.6H_2O$) and ammonium dibasic phosphate ($(NH_4)_2HPO_4$). The procedure is given as follows. A 5 ml of 1 M solution of each of nickel nitrate and dibasic ammonium hydrogen phosphate were mixed together at room temperature in a round bottom flask with continuous gentle stirring. Directly after mixing a greenish precipitate is formed. Few drops of conc. Nitric acid were added to dissolve the precipitate to get a uniform clear solution. A 50 ml of 0.3 M urea solution was added to the homogenous mixture. The round flask was connected to a condenser and maintained at a definite refluxing temperature of 80 °C with a uniform stirring for 15 h. After refluxing process, a greenish suspension was obtained and left to cool to room temperature, then filtered and washed several times with bi-distilled water. Finally, the precipitate was left in an oven at 80 °C to dry for overnight to be ready for different characterizations.

The catalyst ink of nickel phosphate nanoparticles (NiPh), for being anchored on the surface of glassy carbon electrode (GC), was prepared by adding the proper mass (to obtain

specific loading level, see section 2.2) of the NiPh powder in a test tube containing 2.5 ml isopropanol + 50 μL of Nafion solution (5% in water). The above mixture was sonicated for 30 min in an ice bath.

Electrode Modification

Glassy carbon electrode, GC (d = 2 mm) is used here as the underlying substrate for nickel phosphate particles. It was cleaned by mechanical polishing with aqueous slurries of successively finer alumina powder (down to 0.06 μm), then washed thoroughly with second distilled water and then ethanol. Next, 25 μL of freshly prepared NiPh suspension (prepared as given above) is casted onto the thus cleaned GC electrode and left overnight for drying in air. The prepared loading levels were 1.59, 3.18, 4.77, 6.37, 7.96 mg cm^{-2} (of the electrode surface area).

Measurements

The phase structure of the synthesized product was studied using X-ray diffraction (XRD). The XRD pattern was obtained using a diffractometer ((PANalytical, X'Pert PRO) equipped with a Cu Ka radiation (λ =1.5406 A^o). XRD radiation generated at 40KV and a current of 44 mA with a scan rate of 2^o/min over range of 4-80^o. The infrared spectra (FT-IR) was performed by using JASCO 3600 spectrophotometer using ca. 0.5 mm KBr pellets containing 2.5 wt.% sample. The morphology of the NiPh samples was investigated using scanning electronic microscopy (SEM, Model JEOL JSM 5410, Japan). The BET specific surface areas of the samples were examined using low-temperature (77.38 K) nitrogen adsorption isotherms measured over a wide range of relative pressures from 0.02 to 0.9 atm. Adsorption measurements were performed on a Micromeritics ASAP2010 volumetric adsorption apparatus. High-purity nitrogen (99.9999%) was used. Prior to measurement, the samples were degassed at 40 °C for 18 h in the degas pot of the adsorption analyzer.

Electrochemical measurements were performed using Gamry potentiostat/galvanostat supported with Gamry electrochemical analysis technique. Electrochemical measurements were carried out in a conventional three-electrode cell. The counter electrode was made of a platinum coil. The reference electrode was Ag/AgCl/KCl (sat.) with a Luggin probe positioned near the electrode surface. The potential throughout the text is referred to the above reference electrode. The reproducibility of the results of glucose oxidation was evaluated by taking three measurements for the same electrode prepared three different times (n = 3 (or three CVs)) and estimating the relative standard deviation (RSD) (*c.f.* Figs. 7c and 8b).

Results and Discussion

Morphology and Structure of the NiPh

The thus prepared nickel phosphate particles were characterized using different techniques in order to investigate the morphology and structure of the substance. Fig. 1 shows the SEM micro images of the NiPh. The image demonstrates that there is a coagulation of particles that formed with needle-like morphology and had an average particle size of 200 × 800 nm. It may be concluded that the material is one-dimensional nanomaterial. The particle size is uniform with some coagulation due to aggregation of the powder due to hygroscopic nature of the substance.

The chemical structure of the prepared NiPh was identified by FT-IR absorption spectroscopy and XRD pattern. Fig. 2 shows the FT-IR spectrum for NiPh in the range of wave number between 3500 and 400 cm^{-1}. Different sets of bands are seen in Fig. 2. These bands are corresponding to different functional groups as follows. The figure reveals that there are three vibrational broad bands in the range of 3000 to 3450 cm^{-1} (from 1 to 2 peaks) assigned to the O-H stretching vibration of the H_2O that was validated by XRD (*c.f.* Fig. 3). The bending vibrational mode of water molecules appear at 1592 cm^{-1} (peak 3) [53, 54]. The band assigned at 740 cm^{-1} (peak 3) is attributed to the vibrational modes of water molecules. Based on literatures, those bands were disappeared when nickel phosphate were calcined at higher temperatures [55]. The vibrational bands of PO_4^{3-} anion are observed at 1072, 1022, 991 and 883 cm^{-1} (peaks 4, 5, 6 and 7) [53, 54]. Those bands are corresponding to the tetrahedral PO_4^{3-}

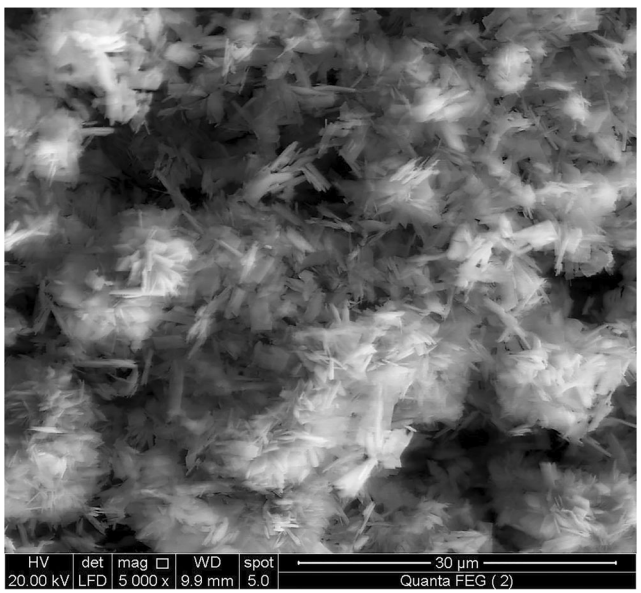

Fig. 1 SEM image of the NiPh

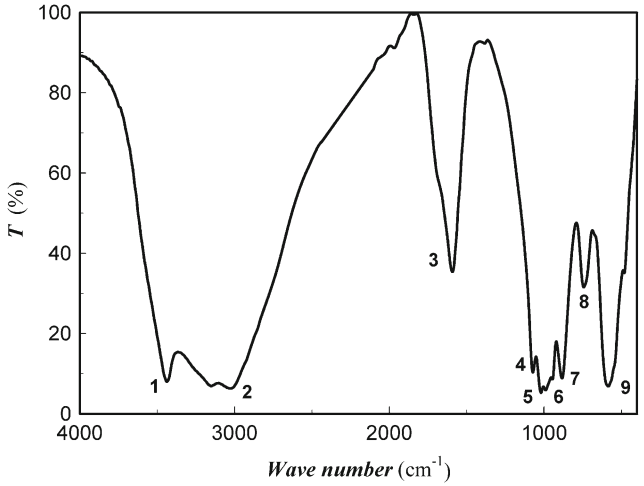

Fig. 2 FTIR spectrum of the NiPh

stretching vibrations, and the strong band around 580 cm^{-1} (peak 9) is assigned to the P–O vibrations.

To confirm the above findings of the FT-IR spectrum, the XRD pattern of the NiPh was measured for the prepared powder. The pattern is shown in Fig. 3. Compared to the standard spectrum (PDF No. 33–0951) the obtained spectrum for these synthesized materials demonstrates that the chemical identity of the nickel phosphate in the form of $Ni_3(PO_4)_2.8H_2O$ and having a monoclinic crystallographic form [56]. The crystallinity and purity of the prepared nickel phosphate sample were examined by X-ray diffraction (XRD) pattern. The XRD pattern consists of sets of peaks which are corresponding only to NiPh. Also, the XRD pattern shows that the samples are generally produced in a single phase structure. The average grain size D is estimated by means of the Scherrer formula; [57]

$$D_{hkl} = k\lambda/\beta\cos\theta \quad (1)$$

where, D_{hkl} is the average crystallite size, k is a constant shape factor ≈ 0.9, β is the full width at half maximum, λ is the wavelength of the X-ray radiation, θ is the angle of diffraction.

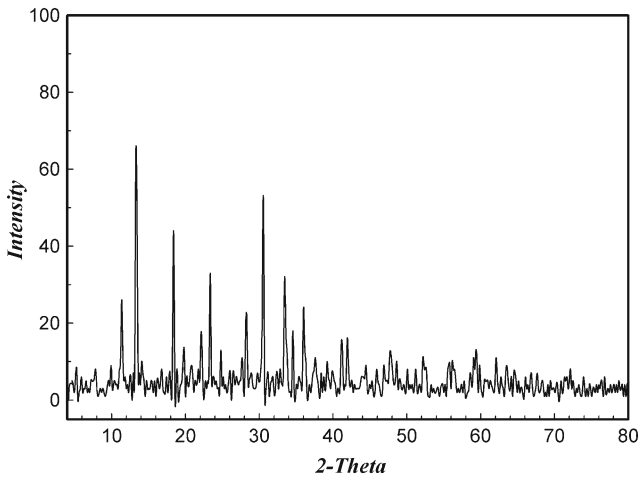

Fig. 3 The XRD pattern of the prepared NiPh

The average grain size D_{hkl} is estimated to be 51.0 nm for the NiPh prepared by the present experimental conditions. The surface area of the NiPh powder formed by reflux method was given by BET method. It was found that the formed particles had a specific surface area of 19.5 m^2/g. Additionally, the total pore volume and the average pore size for the produced nickel phosphate powdered were 7.0×10^{-3} cm^3/g and 12.0 nm respectively.

Electrochemical Characteristics of NiPh/GC

As obtained from the XRD data, the oxidation state of the nickel phosphate ($Ni_3(PO_4)_2.8H_2O$) is in a divalent state. To investigate the electrochemical activity, the electrochemical pretreatment studies should be handled. These studies can be achieved by running a potential cycling of the NiPh/GC in alkaline solution (0.25 M KOH) in the range from −0.1 V to 0.7 V (Ag/AgCl/KCl) at scan rate of 100 mV s^{-1}. In the beginning (first cycle) of the cyclic voltammogram, the CV (CVs are not shown here) data did not show any peaks but when more cycling has been done for the electrode at the same potential range, a pair of peaks begun to appear in the range of 0.46 to 0.57 V (*c.f.* Fig. 4). Those peaks reveal that the peak current for both anodic and cathodic sweeps increases with the potential cycling. This procedure and the consequent appearance of that redox peaks are obtained for all NiPh loadings. Therefore, there is similarity in the CV responses obtained for all loadings as shown in Fig.4. The different used loadings of the NiPh are; (a) 1.59, (b) 3.18, (c) 4.77, (d) 6.37, (e) 7.96 mg cm^{-2} (of the electrode surface area). It is shown in Fig. 4 that a couple of peaks was obtained after cycle number ~ 75 at the different loading values. The position of the peak potentials fairly depends on the loading extent. For instance, at loading of 4.77 mg cm^{-2} (curve c), this couple of these peaks appear at

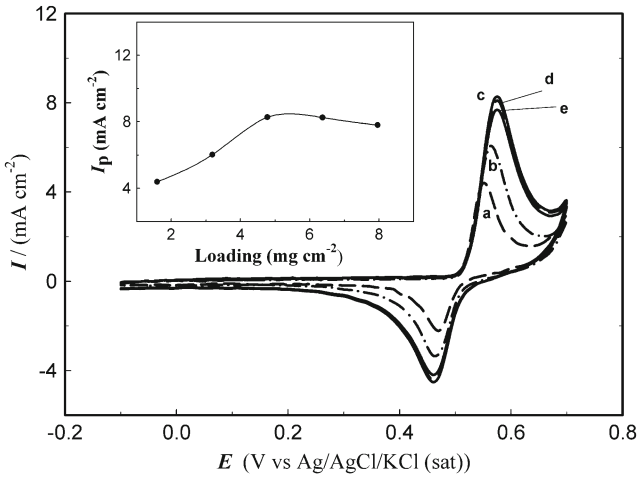

Fig. 4 CV responses of NiPh/GC in blank 0.25 M KOH at different NiPh loadings at scan rate of 100 mV s^{-1}. The different loadings are: a 1.59, b 3.18, c 4.77, d 6.37 and e 7.96 mg cm^{-2} (of the electrode surface area). The inset shows the relation between I_p and the loading level

0.57 V for the anodic sweep and at 0.46 V for the cathodic sweep. These peaks can be assigned for the Ni (II)/Ni (III) transform according to following equation

$$Ni_3(PO_4)_2 + 3OH^- \rightarrow Ni_3(OH)_3(PO_4)_2 + 3e \quad (2)$$

This includes the invasion of the hydroxide ions to the NiPh matrix during the potential cycling and formation of Ni (II) Ph (i.e., $Ni_3(PO_4)_2$) and Ni (III) Ph (i.e., $Ni_3(OH)_3(PO_4)_2$). During the potential cycling, the matrix is gradually getting enriched with the Ni (II) Ph and Ni (III) Ph species until it reaches constant surface concentration at cycle number ~ 75. After reaching the saturation level, the diffusion of the OH^- ions into the phosphate matrix becomes a controlling factor and hence no further increase in the peak currents was observed at higher loadings.

As the loading level increases, both the anodic and cathodic peak currents increase up to loading level of 4.77 mg cm^{-2}. After that loading level, the data did not show any variations in the CV responses. The inset of Fig. 4, for instance, shows a relation between the anodic peak current, I_{pa} with the loadings. It can be noticed that the peak current is increased to a certain limit and then almost levels off with a constant value when the loading of the catalyst goes above a value of 4.77 mg cm^{-2}. It may be concluded that a loading level of 4.77 mg cm^{-2} is considered to be an optimum loading for this electrode at the present experimental conditions and it will be used in the rest of all studies of this work.

Figure 5a shows CV responses of the NiPh/GC in 0.25 M KOH at different potential scan rates using loading of 4.77 mg cm^{-2}. As the scan rate increases, the peak current both in the anodic and cathodic sweeps increases. The anodic peak potential shifts to more positive values and the cathodic peak potential shifts to more negative values. This result points to the quasi-reversible nature of the Ni (II)Ph/Ni (III)Ph transformation. A plot of the peak current, I_p for both anodic and cathodic peaks with the scan rate, ν is shown in Fig. 5b. A straight line is obtained in both cases. However, lower obtainable current values were seen in the cathodic peak. These results indicate that the redox transformation, Ni(II)Ph/Ni(III)Ph is a surface-confined process. The surface concentration of the active NiPh species, Γ, was estimated from the equation:

$$\Gamma = \frac{Q}{nF} \quad (3)$$

where Q is the charge passed during the Ni (II)/Ni (III) transformation, n is the number of electrons and F is Faraday's constant. The quantity of charge, Q was estimated by integration of the area under the anodic sweep at scan rate of 5 mV s^{-1} in Fig. 5a. This was estimated for the Ni (II)Ph/Ni (III) Ph (n = 3, see Eq. 2). The value of Γ was found to be 1.73×10^{-4} mmol cm^{-2} for the Ni (II)Ph/Ni (III) Ph at the present loading level (4.77 mg cm^{-2}). Thus the loading level in mg cm^{-2} can be obtained from the above value of Γ using the following formula:

$$\text{Estimated loading } \left(\text{mg cm}^{-2}\right) = \Gamma \times \text{M}\left(\text{NiPh}_{\text{Avg}}\right) \quad (4)$$

where M ($NiPh_{Avg}$) is the average molar mass in g/mol for the nickel species which was calculated as the average between the $Ni_3(PO_4)_2$ and $Ni_3(OH)_3(PO_4)_2$. The loading level estimated from Eq. 4 is 0.045 mg cm^{-2}. This value is less than the real loading level (4.77 mg cm^{-2}) and yet the percentage utilization ([Estimated loading/real loading] × 100) is ~1.0%. This value is a characteristic for the surface nature of the activation process and indicative for low penetration extent. Also, it may be concluded that the conversion of the NiPh to redox couple is limited to some surface layers.

Electrocatalytic Oxidation of Glucose:

Figure 6 depicts CV responses for NiPh/GC in 0.25 M KOH in the presence and absence of a 20 mM glucose solution at scan rate of 20 mV s^{-1}. In the absence of glucose (curve a), the CV data shows two peaks, the anodic peak appears at 0.52 V but the cathodic peak occurs at 0.45 V. These peaks can be assigned to the redox transforming of Ni (II)Ph/Ni (III) Ph as discussed previously (see Eq. (2)). Where Ni (II) ➔ Ni (III) transform takes place in the anodic sweep, the Ni (III) ➔ Ni (II) transform takes place in the cathodic sweep. On the other hand in presence of glucose (curve b), the anodic current rises dramatically and the anodic peak potential is observed at ~0.6 V. This peak is assigned for electrooxidation of glucose at the present conditions. It is noticed that the cathodic peak of the Ni (III) ➔ Ni (II) transform (curve "b", the reverse weep) is extremely diminishes which may point to the electrocatalytic nature of the glucose oxidation. In the reverse sweep (see arrows), another anodic peak in the reverse direction appears at almost the same peak potential but with lower peak current. This is due to further glucose oxidation on the regenerated NiPh sites. Since the current of anodic glucose oxidation in the reverse weep is lower than that in the forward sweep, it may be concluded that the active sites were not fully recovered. The disappearance of the cathodic peak suggests an irreversible electrocatalytic oxidation of glucose [58, 59].

Analysis of the glucose oxidation on NiPh/GC electrode can be achieved by collecting CV responses at various potential scan rates. Figure 7a depicts the CV responses of the NiPh/GC in 0.25 M KOH containing 10 mM glucose at different scan rates in the range from 5 to 400 mV s^{-1}. It is noticed that the peak potential of glucose oxidation shifts to more positive values with the san rate. This may suggest kinetic limitation of the glucose electrocatalytic oxidation on the NiPh/GC electrode. In the presence of relatively high concentration of the

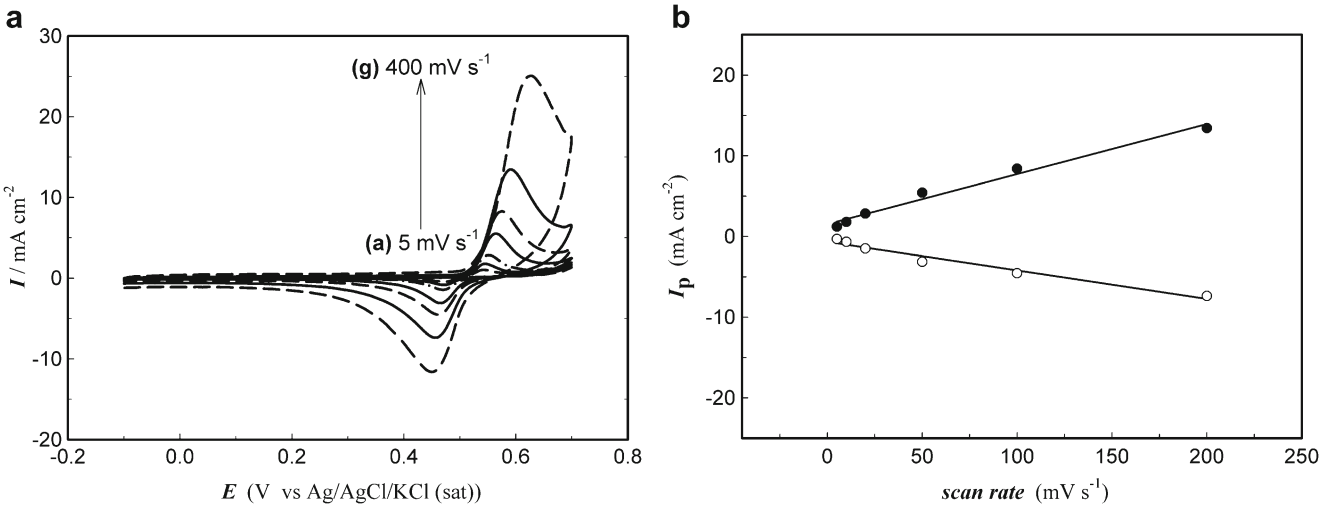

Fig. 5 a CV responses of the NiPh/GC in blank 0.25 M KOH at different potential scan rates in the range of 5 to 400 mV s^{-1}. a 5, b 10, c 20, d 50, e 100, f 200 and g 400 mV s^{-1} and b Plots of I_{pa} and I_{pc} against the scan rate, ν (the data are extracted from Fig. 5a). (●) is the anodic and (○) is the cathodic branch

electrolyte (0.25 M KOH) with respect to the glucose oxidation (10 mM), the positive shift in potential due to ohmic drop can be excluded in this case. The anodic peak current, I_p of glucose oxidation increases with the scan rate and the cathodic peak diminishes compared to the CV response in the blank (see Fig. 6). However, the degree of disappearance of the cathodic peak depends on the scan rate. As the scan rate increases the cathodic peak becomes more obvious and yet some of the Ni (III) Ph sites are not consumed at the high scan rates. A plot of the peak potential, E_p with the logarithm of the scan rate, ν is shown in Fig. 7b. The plot demonstrates a straight line and can be fitted with the following equation; [60, 61]

$$E_p = K + \frac{2.303\,RT}{2\alpha n_a\ F}\log\nu \tag{5}$$

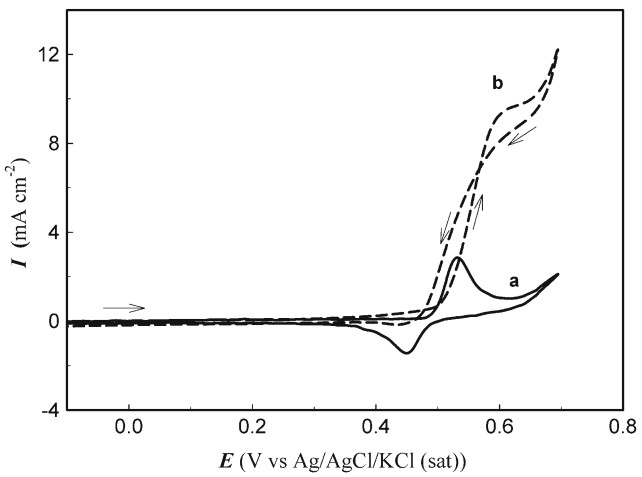

Fig. 6 CV responses of NiPh/GC in blank 0.25 M KOH a and in 0.25 M KOH containing 20 mM Glucose b at scan rate of 20 mV s^{-1}

where K is a constant given by:

$$K = E^o + \frac{RT}{2\alpha n_a F}x\left[0.78 + 1.15\ \log\left(\frac{\alpha n_a FD}{k^2 RT}\right)\right] \tag{6}$$

The parameters in the above equations are defined as follows: α is the charge transfer coefficient, n_a is the number of electrons evolved in the rate determining step, E^o is the standard electrode potential, k is the heterogeneous rate constant and D is the diffusion coefficient. The straight line shown in Fig. 7b gives a slope of 0.055 V and from which the value of αn_a is found to be 0.566. This value is closer to the values found in literatures for which system at similar conditions [62].

Figure 7c illustrates the relation between I_p for glucose oxidation with the square root of the scan rate, ν. The values of I_p were extracted from the CVs in Fig. 7a. The RSD values of range from 2 to 3% are obtained which points to good reproducibility (see the Experimental section). A straight line is obtained in Fig. 7c (R^2 = 0.997). This can lead to a conclusion that glucose oxidation on the NiPh/GC is diffusion-controlled and consequently Randles-Sevcik equation can be applied for diffusion-controlled totally irreversible process (Eq. (7)) [63, 64]:

$$I_p\ = 0.4961\,xnF\left(\frac{\alpha n_a FD}{RT}\right)^{0.5} AC\nu^{0.5} \tag{7}$$

where n is the total number of electrons (n = 2) [15], A is the surface area of the working electrode, D is the diffusion coefficient of glucose C is the bulk concentration of glucose and ν is the potential scan rate. Also, F is the Faraday's constant, R is

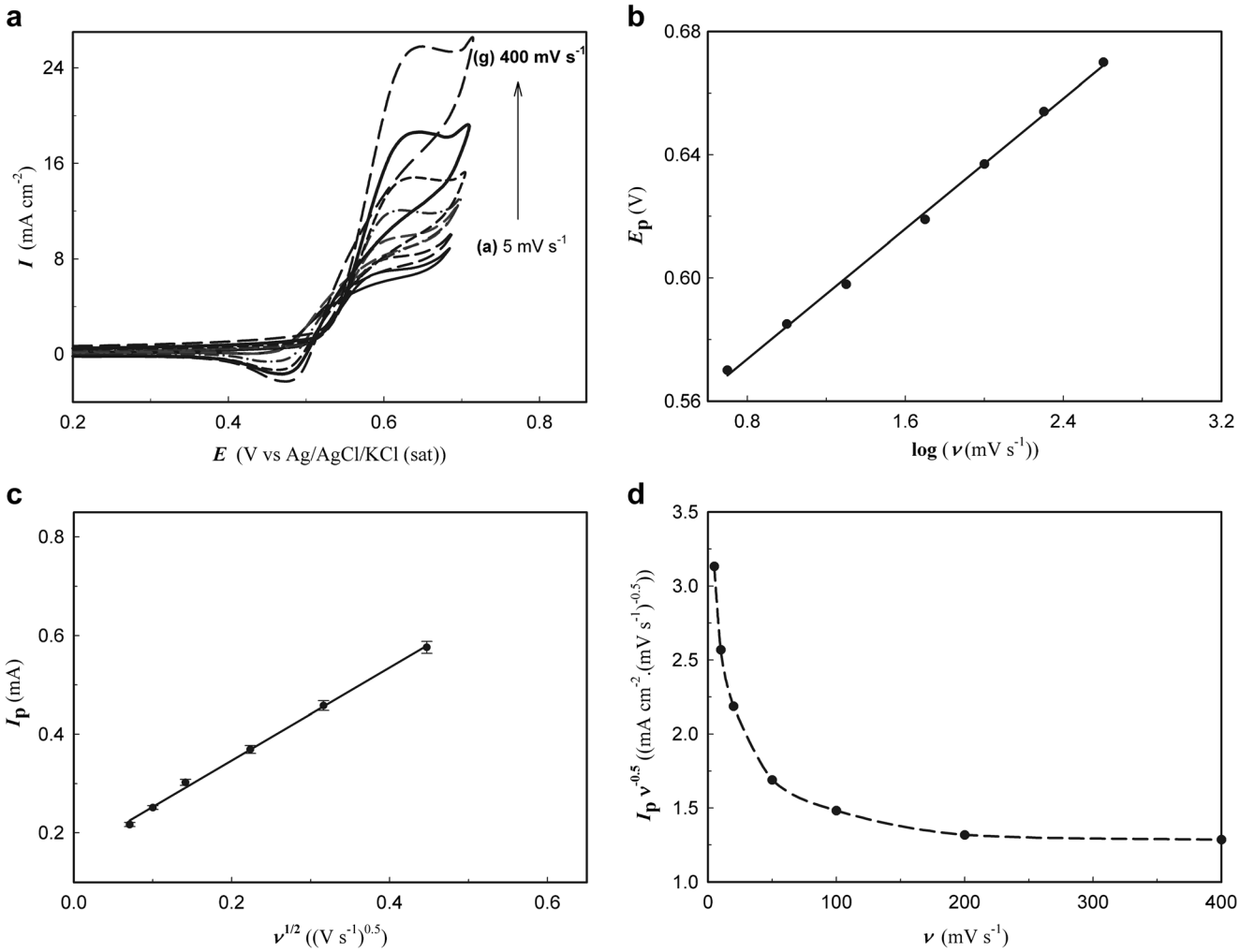

Fig. 7 a CV responses of NiPh/GC in 0.25 M KOH containing 10 mM glucose at different potential scan rates in the range of 5 to 400 mV s^{-1}. a 5, b 10, c 20, d 50, e 100, f 200 and g 400 mV s^{-1}, b Plot of anodic peak potential, E_p and logarithm of the scan rate, log ν, c Anodic peak current, I_p with $\nu^{0.5}$. The uncertainty bars show the standard deviation and d the relation between I_p. $\nu^{-0.5}$ with the scan rate, ν

the gas constant and T is the absolute temperature. From the slope of the obtained straight line in Fig. 7c, the diffusion coefficient was found to be 8.5×10^{-6} cm^2 s^{-1}. The literature value is 6.7×10^{-6} cm^2 s^{-1} and hence the value of D obtained from this work is comparable to those obtained in literatures [65, 66]. Further analysis of the data in Fig. 7a may give us an insight into glucose oxidation process. This was done by plotting $I_p.\nu^{-0.5}$ with the scan rate as shown in Fig. 7d. The curve demonstrates the characteristics profile of typical electrocatalyst regeneration mechanism. Then it is possible to say that the catalyst regeneration mechanism of the electrocatalytic oxidation of glucose performed in this work is in accordance with those in literature for Ni (II)/Ni (III)-based catalyst [67].

Figure 8a represents CVs of NiPh/GC at different glucose concentrations with a scan rate of 20 mV s^{-1}. The figure shows that there is a limiting correlation between the peak current of glucose oxidation and its concentration. As the glucose concentration increases to a certain limit, the peak current of the glucose oxidation increases in a manner depends on the range of the glucose concentration. The data also shows that the increase in the peak current at [glucose] > 40 mM is not significant although the [glucose] is increased to its doubled value (i.e., from 40 mM to 80 mM). A plot of the I_p of glucose oxidation with the [glucose] is given in Fig. 8b. The peak current increases linearly with the [glucose] up to concentration ≤ 20 mM before it deviates from this linearity at [glucose] ≥ 20 mM. Also, a lower sensitivity of the peak current with the glucose concentration is observed at [glucose] ≥ 20 mM. It may be concluded that the glucose oxidation at [glucose] ≤ 20 mM proceed under a diffusion-controlled regime. However, at higher glucose concentrations, the peak current tends to have different mode indicating a limitation in the kinetics of the glucose oxidation process [68]. That deviation can be explained as follows. Glucose in

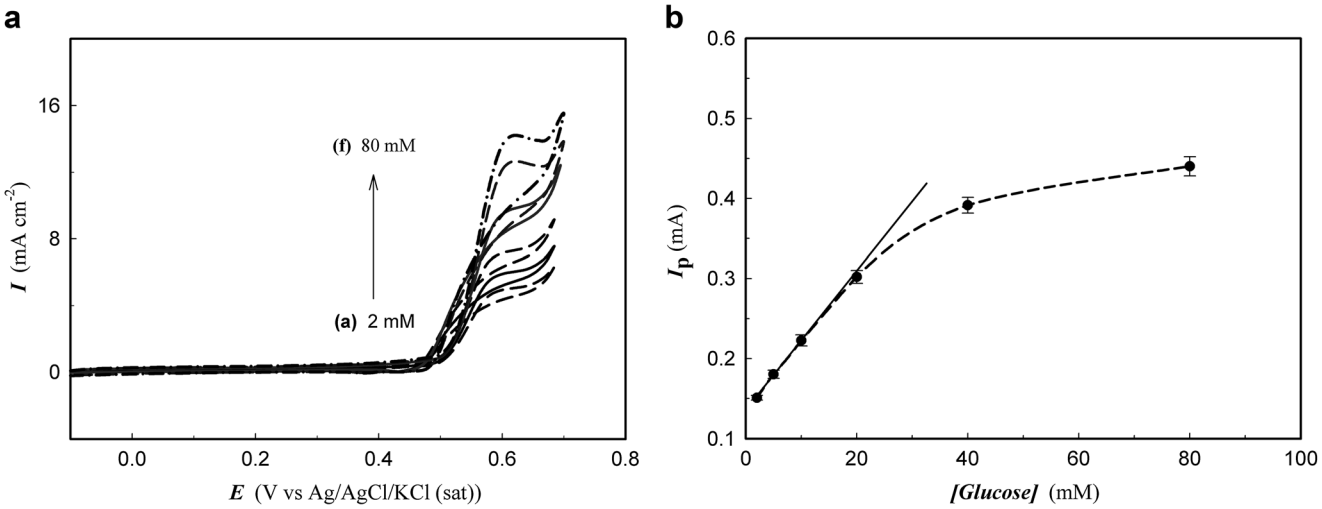

Fig. 8 CV responses of NiPh/GC in 0.25 M KOH containing different glucose concentrations at scan rate of 20 mV s^{-1}. a 2, b 5, c 10, d 20, e 40 and f 80 mM glucose. The inset shows the relation between I_p of glucose oxidation with the glucose concentration, [glucose]. The uncertainty bars show the standard deviation

alkaline solution spontaneously isomerizes mainly to fructose. The latter is known to have lower performance than glucose [69]. Also, the role of the poisoning intermediates cannot be excluded [70]. Moreover, as the hydroxide ions, OH^- has an essential role in electrooxidation of small organic molecules [71]; it is of obvious reason to attain some free fraction of the electrode surface for OH^- adsorption. At this high glucose concentration ([glucose] ≥ 20 mM), the glucose is considered to be a competitive adsorbate with the OH^- ions and hence this competitive adsorption of glucose plays an essential negative role [72].

Stability of an electrocatalyst towards electrochemical oxidation of organic molecules is an essential issue to be addressed for possible use in fuel cells and biochemical sensors. Fig. 9a shows current-time relation (*I-t*) of NiPh/GC in 0.25 M KOH containing 20 mM glucose at E = 0.6 V. As the curve demonstrates an initial increase of the current due to initial activation of the electrode is followed by a decrease to stable currents. This result denotes continuous enhancement of the glucose oxidation at a considerably long duration of ~1.0 h. This result demonstrates considerable stability of the NiPh/GC towards glucose electrooxidation at the present experimental conditions.

The data presented here is a first trial for using nickel phosphate (NiPh) (and maybe for nickel inorganic salt) as an electrocatalyst for glucose from alkaline electrolyte. Also, it is evident from the results of this work and others that the electrooxidation of small organic molecules follows catalyst-regeneration mechanism. Generally, NiPh is bearing redox properties only after potential cycling in the alkaline KOH solution. Where the production of the Ni (II) Ph and Ni (III) Ph is a vital evident from the characteristics CVs (Fig. 5). The enrichment of the nickel phosphate matrix offering considerable concentration of the redox species Ni (II) and Ni (III) which was enough for electrocatalytic oxidation of glucose under the prevailing conditions. Catalyst-regeneration mechanism for glucose oxidation may be written as: [72, 73]

$$2\mathrm{Ni(II)} + 6OH^- \rightarrow 2\mathrm{Ni(III)(OH)_3} + 6e^- \quad (8)$$

$$2\mathrm{Ni(III)(OH)_3} + 3\ \mathrm{Glucose} \rightarrow 2\mathrm{Ni(II)} + 3\ \mathrm{gluconolactone} + 6OH^- \quad (9)$$

The above conversion of glucose to gluconolactone may be proved by plotting Cottrell equation which is given by;

$$I = nFA\ D^{0.5} C\, \pi^{-0.5} t^{-0.5} \quad (10)$$

Where n is the number of electrons needed for the conversion of one molecule of glucose and the t is the time in seconds (s) and the rest of parameters has the same meanings as in Eq. (7). Figure 9b shows the chronoamperometric curve of glucose oxidation on the NiPh/GC electrode from 0.25 M KOH containing 20 mM of glucose at E = 0.6 V. The onset shows a plot of the current, I with $t^{-0.5}$. The plot reveals a straight line (R^2 = 0.995). From the slope of that line, the value of n was found to be 2.23 (~ 2.0). This means that one molecule of glucose needs two electron to be converted to gluconolactone which may be an evidence of that conversion. The above results are in agreement with several literatures [see for instance [73, 74]].

It may be concluded that glucose molecule combine with oxidation state (Ni (III)) (higher oxidation states) converting them to Ni (II) (lower oxidation states). The latter (Ni (II)) is re-oxidized to give again the higher oxidation state (Ni (III)

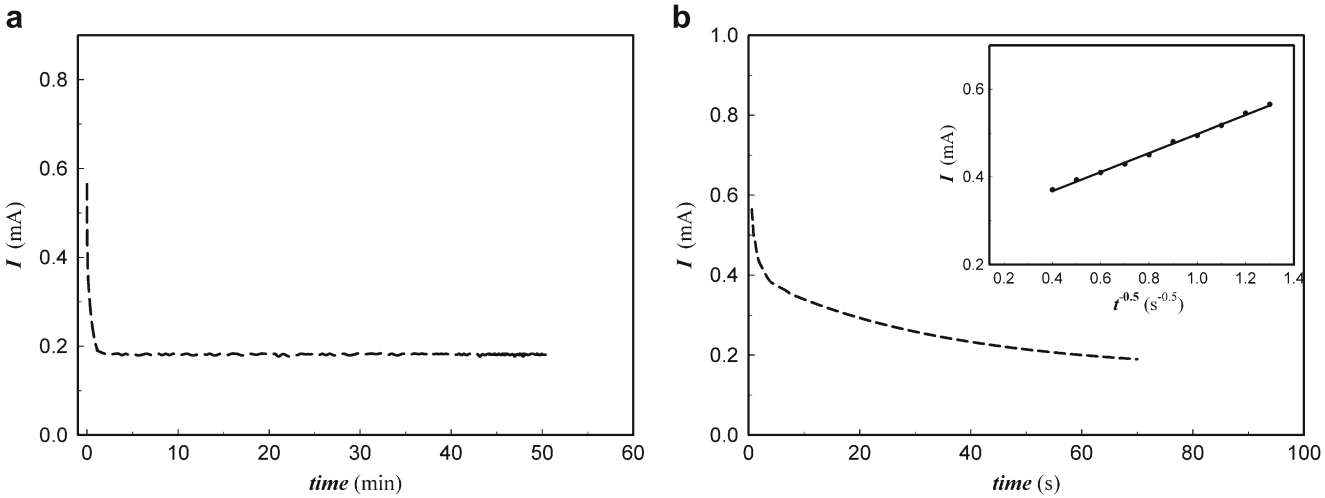

Fig. 9 a *I-t* curve for glucose electrooxidation on NiPh/GC in 0.25 M KOH containing 20 mM glucose and b Chronoamperometric curve and the inset shows the $I\text{-}t^{-0.5}$ plot for glucose oxidation from 0.25 M KOH containing 20 mM glucose at E = 0.6 V

due to the existing high anodic potential. Consequently, in the reverse sweep (see Fig. 6), the catalytically active Ni (III) further oxidizes glucose and be reduced to Ni (II). Meanwhile, glucose is chemically oxidized to products. The inactive Ni (II) will be electrochemically oxidized to Ni (III) due to the prevailing high oxidation potential and thus regenerating the catalyst for further oxidation of glucose molecules. The results shown so far demonstrate electrocatalytic activity of the NiPh/GC for glucose oxidation. However, a comparison with the current used catalysts for the same purpose is presented here. The peak current and peak potential in the present work was compared with some literatures values at similar conditions. It was found that our values are better than those for; Ni $(OH)_2$/Zeolite/GC [74], CuO/NiO/FTO [75], Ni $(OH)_2$/ITO [76], Ni $(OH)_2$/Chitosan/GC [77], Ni-Co/GO/GC [78], porous-NiO/Ni [79], GO/NiO/GC [80], NiO_x/GC [81], CuO/Cu [82], NiO/MWCNT/GC [53], Cu/ZnO [83] and Cu (nanowires)/GC [84]. Meanwhile, our values are equal or less than those for; Ni/GC [72], Ni(II)-quercetin/MWCNT [68], NiOx (sol-gel)/GC [15], Au/GC [85, 86] and Pt/GC [87, 88]. The present study shows that the (NiPh/GC) was found to be superior to many electrodes and it is normal to have less performance compared to master electrocatalysts such as Pt and Au. The above electrocatalytic activity of NiPh/GC may be correlated to the high adsorbability of the phosphate ions, PO_4^{3-} to the small organic compounds [89] and better stability of the Ni (II)/Ni(III) active sites due to the backbone of the phosphate structure [33] which are advantages for using NiPh as an electrocatalyst. The present work introduces a new catalyst (NiPh) for oxidation of glucose (important catalytic reaction in fuel cells and biosensors) and it may present a valuable contribution to the electrocatalysis field.

Conclusions

Nickel phosphate was produced by a reflux-based route and characterized by different techniques including: field emission scanning electron microscopy (FE-SEM), X-ray diffraction (XRD) and FTIR spectroscopy. According to the above measurements, the obtained phase structure for NiPh particles is $Ni_3(PO_4)_2.8H_2O$ with a needle-like morphology with average particle dimensions of 200 × 800 nm. The modified electrode NiPh/GC was characterized by cyclic voltammetry. Electrochemical Activation of the NiPh/GC was achieved in 0.25 M KOH by using potential cycling. The salt, NiPh is bearing redox couple (Ni (II)/Ni (III)) only after the above activation method. Electrocatalytic oxidation of glucose was reported for the first time on NiPh/GC and the modified electrode showed high activity under the present experimental conditions. The glucose oxidation process was analyzed and important transport and kinetic parameters were extracted.

References

1. X. Tang, B. Zhang, C. Xiao, H. Zhou, X. Wang, D. He, Sensors Actuators B **222**, 232–239 (2016)
2. S.B. Bankar, M.V. Bule, R.S. Singhal, L. Ananthanarayan, Biotechnol. Adv. **27**, 489–501 (2009)
3. R.D. Milton, K. Lim, D.P. Hickey, S.D. Minteer, Bioelectrochemistry **106**, 56–63 (2015)
4. S. Guo, E. Wang, Nano Today **6**, 240–264 (2011)
5. N. Torto, Bioelectrochemistry **76**, 195–200 (2009)
6. K.W. Yuan, X. Xia, Adv. Funct. Mater. **15**, 803–809 (2005)
7. M. Guo, H. Fang, H. Hong, N. Tang, X. Xu, Electrochim. Acta **63**, 1–8 (2012)
8. J. Yang, M. Cho, Y. Lee, Sensors Actuators B **222**, 674–681 (2016)

9. M. Chawla, V. Sharma, J.K. Randhawa, Electrocatalysis **8**, 27–35 (2017)
10. Y. Gu, H. Yang, B. Li, Y. An, Electrochim. Acta **192**, 296–302 (2016)
11. Y. Miao, L. Ouyang, S. Zhou, L. Xu, Z. Yang, M. Xiao, R. Ouyang, Biosens. Bioelectron. **53**, 428–439 (2014)
12. G. Vertes, G. Horanyi, J. Electroanal. Chem. **52**, 47–53 (1974)
13. Y. Mu, D. Jia, Y. He, Y. Miao, H.L. Wu, Biosens. Bioelectron. **26**, 2948–2952 (2011)
14. A. Safavia, N. Malekia, E. Farjami, Biosens. Bioelectron. **24**, 1655–1660 (2009)
15. A.S. Danial, M.M. Saleh, S.A. Salih, M.I. Awad, J. Power Sources **293**, 101–108 (2015)
16. E. Sharifi, A. Salimi, E. Shams, A. Noorbakhsh, M.K. Amini, Biosens. Bioelectron. **56**, 313–319 (2014)
17. G.W. Lee, S.D. Minteer, J. Electrochemical Society **160**(8), H463–H468 (2013)
18. D. Chen, G.W. Lee, S.D. Mintee, ECS Electrochemistry Letters **2**(2), F9–F13 (2013)
19. P.M. Robertson, P.M. J, Electroanal. Chem. **111**, 97–104 (1980)
20. J.F. Wolf, L.-S.R. Yeh, A. Damjanovic, Electrochim. Acta **26**, 811–817 (1981)
21. L. Ding, A. Wang, G. Li, Z. Liu, W. Zhao, C. Su, Y. Tong, J. Am. Chem. Soc. **13**, 45730–45733 (2012)
22. Y. Kang, W. Wang, Y. Pu, J. Li, D. Chai, Z. Lei, Chem. Eng. J. **308**, 419–427 (2017)
23. R. Ding, X. Li, W. Shi, Q. Xu, L. Wang, H. Jiang, Z. Yang, E. Liu, Electrochim. Acta **222**, 455–462 (2016)
24. X. Wang, W. Li, D. Xiong, D.Y. Petrovykh, L. Liu, Adv. Funct. Mater. **26**, 4067–4077 (2016)
25. A. Abdel Aal, H. B. Hassan, M.A. Abdel Rahim, J. Electroanal. Chem. 619–620, 17–25 (2008)
26. A.-F. Shaol, Z.-B. Wangl, Y.-Y. Chul, Z.-Z. Jiangl, G.-P. Yin, Y. Liu, Fuel Cells **10**, 472–477 (2010)
27. A.R.J. Kucernak, K.F. Fahy, V.N.N. Sundaram, Catal. Today **262**, 48–56 (2016)
28. Y.Y. Tong, C.D. Gu, J.L. Zhang, H. Tang, Y. Li, X.L. Wang, J.P. Tu, Electrochim. Acta **187**, 11–19 (2016)
29. O. A. Rusu, W. F. Hoelderich, H. Wyart, M. Ibert, Appl. Catal. B Environ. 176–177, 139–149 (2015)
30. Z. Yu, Y. Kou, Y. Dai, X. Wang, H. Wei, D. Xia, Electrocatalysis **6**, 341–347 (2015)
31. M.N. Timofeeva, Z. Hasan, A.Y. Orlov, V.N. Panchenko, Y.A. Chesalov, I.E. Soshnikov, S.H. Jhung, Appl. Catal. B Environ. **107**, 197–204 (2011)
32. M.N. Timofeeva, Z. Hasan, V.N. Panchenko, I.P. Prosvirin, Sung Hwa Jhung, J. Molecular Catalysis A: Chemical 363–364, 328–334 (2012)
33. M.M. Saleh, A.H. Touny, M.A., A.l. Omair, M.M. Saleh, Biomed. Mater. Eng. **27**, 87–99 (2016)
34. J. Sánchez-Enríquez, J. Reyes-Gasga, Ultrason. Sonochem. **20**, 948–954 (2013)
35. M.P. Ginebra, T. Traykova, J.A. Planell, J. Control. Release **113**, 102–110 (2006)
36. A.A. Ahmed, A.A. Ali, D.A.R. Mahmoud, A.M. El-Fiqi, Solid State Sci. **13**, 981–992 (2011)
37. L. Cheng, M.D. Weir, H.K. Xu, J.M. Antonuccie, A.M. Kraigsleye, N.J. Line, S. Lin-Gibsone, X. Zhou, Dent. Mater. **28**(5), 561–572 (2012)
38. A. Yamada, S.C. Chung, K. Hinokuma, J. Electrochem. Soc. **148**, A224–A229 (2001)
39. K. Zaghib, K. Striebel, A. Guerfi, J. Shim, M. Armand, M. Gauthier, Electrochim. Acta **50**, 263–270 (2004)
40. X. Zhao, B.M. Sanchez, P.J. Dobson, P.S. Grant, Nano **3**, 839–855 (2011)
41. X. Peng, L. Peng, C. Wu, Y. Xie, Chem. Soc. Rev. **43**, 3303–3323 (2014)
42. S.H. Jhung, J.-H. Lee, A.K. Cheetham, G. Férey, J.-S. Chang, J. Catalysis **239**, 97–104 (2006)
43. Y. Zhan, M. Lu, S. Yang, C. Xu, Z. Liu, J. Yang Lee, Chem CatChem **8**, 372–379 (2016)
44. Y. Liu, L. Zhang, Z. Shi, H. Yuan, W. Pang, J. Solid State Chemistry **158**, 68–73 (2001)
45. X. Wang, Q. Gao, C. Wu, J. Hu, M. Ruan, Mater **85**, 355–364 (2005)
46. S. Jhung, J. Yoon, J. Hwang, A. Cheetham, J. Chang, Chem. Mater. **17**, 4455–4460 (2005)
47. H. Onoda, K. Asai, A. Takenaka, J. Ceramic Processing Research. **12**(4), 439–442 (2011)
48. H. Onoda, T. Ohta, J. Tamaki, K. Kojima, H. Nariai, Mater. Chem. Phys. **96**, 163–169 (2006)
49. J. Yu, A. Wang, J. Tan, X. Li, J. Bokhoven, Mater. Chem. **18**, 3601–3607 (2008)
50. H. Wu, Y. Gaob, H. Li, Cryst. Eng. Comm. **12**, 3607–3611 (2010)
51. S. Lin, S. Chen, S. Cheng, J. Lin, Solid State Sci. **7**, 896–900 (2005)
52. N. Kiraz, E. Burunkaya, O. Kesmez, H. Camurlu, M. Asilturk, Z. Yesil, E. Arpac, J. Sol-Gel Sci. Technol. **59**, 381–386 (2011)
53. S. Kullyakool, C. Danvirutai, K. Siriwong, P. Noisong, Therm. Anal. Calorim. **115**, 1497–1507 (2014)
54. P. Noisong, C. Danvirutai, T. Srithanratana, B. Boonchom, Solid State Sci. **10**, 1598–1604 (2008)
55. C.M. Burba, R. Frech, Spectrochim. Acta A **65**, 44–50 (2006)
56. J. V. Smith (ed.), *X-ray powder data file* (American Society for Testing Materials, Pennsylvania, 1960)
57. G. Feng, S.F. Wang, M.K. Lu, G.J. Zhou, D. Xu, D.R. Yuan, J. Physical Chem. B **108**, 8119 (2004)
58. A.M. Ghonim, B.E. El-Anadouli, M.M. Saleh, Electrochim. Acta **114**, 713 (2013)
59. A.M. Ghonim, B.E. El-Anadoulia, M.M. Saleh, Int. J. Electrochem. Sci. **10**, 612–639 (2016)
60. L. Jiang, R. Wang, X. Li, L. Jiang, G. Lu, Electrochem. Commun. **7**, 597–601 (2005)
61. A.J. Bard, L.R. Faulkner, *Electrochemical methods, fundamentals and application, ed* (John & Sons, Inc, New Jersey, 1980), p. 223
62. M. Shamsipur, M. Najafi, M.R.M. Hosseini, Bioelectrochemistry **77**, 120–124 (2010)
63. J. Wang, *Analytical electrochemistry*, 3rd edn. (John Wiley & Sons, Inc., New Jersey, 2006), p. 34
64. J.J. Zhang, Y.H. Tse, W.J. Pietro, A.B.P. Lever, J. Electroanal. Chem. **406**, 203–211 (1996)
65. N. Torto, T. Ruzgas, L. Gorton, J. Electroanal. Chem. **464**, 252–258 (1999)
66. M.Y. Elahi, H. Heli, S.Z. Bathaie, M.F. Mousavi, J. Solid State Electrochem. **11**, 273–282 (2011)
67. S. Yu, X. Peng, G. Cao, M. Zhou, L. Qiao, J. Yao, H. He, Electrochim. Acta **76**, 512–517 (2012)
68. S. Ci, T. Huang, Z. Wen, S. Cui, S. Mao, D.A. Steeber, J. Chen, Biosens. Bioelectron. **54**, 251–257 (2014)
69. D. Basu, S. Basu, Electrochim. Acta **55**, 5775–5779 (2010)
70. J. McGinley, F.N. McHale, P. Hughes, C.N. Reid, A.P. McHale, Biotechnol. Lett. **26**, 1771–1776 (2004)
71. J. Taraszewska, G. Roslonek, J. Electroanal. Chem. **364**, 209–213 (1994)
72. I. Danaee, M. Jafarian, F. Forouzandeh, F. Gobal, M.G. Mahjani, Electrochim. Acta **53**, 6602–6609 (2008)
73. M. Fleischmann, K. Korinek, D. Pletcher, J. Electroanal, Chem. Interf. Electrochem. **31**, 39–49 (1971)
74. S.K.H. Darzi, M. Rahimnejad, S.N. Mirzababaei, Microchem. J. **128**, 7–17 (2016)
75. F. Cao, S. Guo, H. Ma, G. Yang, S. Yang, J. Gong, Talanta **86**, 214–220 (2011)
76. V. Ganesh, S. Farzana, S. Berchmans, J. Power Sources **196**, 9890–9899 (2011)
77. A. Ciszewski, I. Stepniak, Electrochim. Acta **111**, 185–191 (2013)

78. L. Wanga, X. Lu, Y. Ye, L. Sun, Y. Song, Electrochim. Acta **114**, 484–493 (2013)
79. F.J. Garcia-Garcia, P. Salazar, F. Yubero, A.R. González-Elipe, Electrochim. Acta **201**, 38–44 (2016)
80. Y. Zhang, Y. Wang, J. Jia, J. Wang, Sensors Actuators B 171–172, 580–587 (2012)
81. A.M. Ghoniml, B.E. El-Anadouli, M.M. Saleh, Electrochim. Acta **114**, 713–719 (2013)
82. T.G.S. Babu, T. Ramachandran, Electrochim. Acta **55**, 1612–1618 (2010)
83. S. Ashok Kumar, H.-W. Cheng, S.-M. Chen, S.-F. Wang, Mat. Sci. Eng. **C 30**, 86–91 (2010)
84. Y. Zhang, L. Su, D. Manuzzi, H.V. Espinosa delos Monteros, W. Jia, D. Huo, C. Hou, Y. Lei, Biosens. Bioelectron. **31**, 426–432 (2012)
85. M. Tominag, T. Shimazoe, M. Nagashima, I. Taniguchi, Electrochem. Commun. **7**, 189–193 (2005)
86. S.B. Aoun, Z. Dursun, T. Koga, G.S. Bang, T. Sotomura, I. Taniguchi, J. Electroanal. Chem. **567**, 175–183 (2004)
87. H. Qiu, X. Huang, J. Electroanal. Chem. **643**, 39–45 (2010)
88. L.-H. Li, W.-D. Zhang, J.-S. Ye, Electroanalysis **20**, 2212–2216 (2008)
89. S.J. Yao, S.K.W. Jun, B.K. Ahn, C.C. Liu, Nature **241**, 471–472 (1973)